Phonon and electron contributions to the thermal conductivity of VN_x epitaxial layers

Qiye Zheng,[1,*] Antonio B. Mei,[1] Mohit Tuteja,[1] Davide G. Sangiovanni,[2,3] Lars Hultman,[3] Ivan Petrov,[1,3] J. E. Greene,[1,3] and David G. Cahill[1]

[1]*Department of Materials Science and Engineering, Frederick Seitz Materials Research Laboratory, University of Illinois at Urbana-Champaign, 104 South Goodwin, Urbana, Illinois 61801, USA*

[2]*Atomistic Modelling and Simulation, ICAMS, Ruhr-Universität Bochum, D-44801 Bochum, Germany*

[3]*Department of Physics (IFM), Linköping University, SE-581 83 Linköping, Sweden*

(Received 25 June 2017; revised manuscript received 9 October 2017; published 20 November 2017)

Thermal conductivities of VN_x/MgO(001) ($0.76 \leqslant x \leqslant 1.00$) epitaxial layers, grown by reactive magnetron sputter deposition, are measured in the temperature range $300 < T < 1000$ K using time-domain thermoreflectance (TDTR). Data for the total thermal conductivity are compared to the electronic contribution to the thermal conductivity calculated from the measured electrical conductivity, the Wiedemann-Franz law, and an estimate of the temperature dependence of the Lorenz number $L(T)$. The total thermal conductivity is dominated by electron contribution and varies between 13 $W m^{-1} K^{-1}$ at $x = 0.76$ and 20 $W m^{-1} K^{-1}$ at $x = 1.00$ for $T = 300$ K and between 25 and 35 $W m^{-1} K^{-1}$ for $T = 1000$ K. The lattice thermal conductivity vs x ranges from 5 to 7 $W m^{-1} K^{-1}$ at 300 K and decreases by 20% at 500 K. The low magnitude and weak temperature dependence of the lattice thermal conductivity are attributed to strong electron-phonon coupling in VN.

DOI: 10.1103/PhysRevMaterials.1.065002

I. INTRODUCTION

The phonon contribution to the thermal conductivity of a metal has a complex dependence on temperature, lattice anharmonicity, and the strength of electron-phonon coupling [1–3]. Typically, at temperatures greater than 1/3 of the Debye temperature, the lifetimes of phonons that dominate heat transport are limited by the anharmonicity of lattice vibrations [4]. Scattering of phonons by electrons is typically less important except at low phonon frequencies. Measurements of the thermal conductivity of alloys can often be used to determine the lattice thermal conductivity by introducing elastic scattering of electrons that suppresses the electronic component [5,6]. The high-temperature lattice thermal conductivities of metals with relatively weak electron-phonon coupling are typically in good agreement with the assumption of lattice thermal conductivity limited by anharmonicity [3].

Metallic transition-metal (TM) nitrides and carbides provide a contrast to metals for studying lattice thermal conductivities because their Debye temperatures are high and therefore the anharmonic phonon scattering rates are low, and electron-phonon coupling is strong [7]. The spectral integral of the Eliashberg function $\alpha^2 F(\omega)$ yields a measure of the electron-phonon coupling strength: $\lambda = 2\int \alpha^2 F(\omega)\omega^{-1} d\omega$ [8–10]. For TM nitrides and carbides, λ is between 0.6 and 0.9, large values compared to common metals such as Al ($\lambda = 0.44$), Cu (0.13), Au (0.17), and Ti (0.38) [11,12]. The primary goal of this work is to determine the lattice contribution to the thermal conductivity of VN through studies of the thermal conductivity of stoichiometric VN and VN_x with varying concentrations of nitrogen vacancies.

In Fig. 1(a) we compare representative data for the total thermal conductivities of elemental metals to selected data for TM nitrides and carbides. The temperature dependence of the thermal conductivity of TM nitrides and carbides has been discussed previously [20,24]. Figure 1(b) summarizes the electrical resistivity of the same set of elemental metals and TM nitrides and carbides. In most cases, at temperatures greater than the Debye temperature Θ_D, the resistivity can be approximated as $\rho \approx \rho_0 + B + AT$, wherein we have distinguished between the residual resistivity ρ_0 created by elastic scattering by defects and a phenomenological constant B that describes the shift in the extrapolated intercept of ρ at $T = 0$ K relative to ρ_0.

The Wiedemann-Franz (WF) law predicts that the electronic thermal conductivity can be expressed as

$$\Lambda_{el} \approx \frac{L(T)T}{\rho} = \frac{L(T)T}{\rho_0 + B + AT}. \quad (1)$$

$L(T)$ is the temperature-dependent Lorenz number [25,26]. At low ($T \ll \Theta_D$) and high temperatures ($T \geqslant \Theta_D$), $L(T)$ approaches the Sommerfeld value of $L_0 = 2.44 \times 10^{-8}\,\Omega\,W\,K^{-2}$. In pure metallic elements at $T > \Theta_D/3$, the resistivity typically scales as $\rho \approx AT$ and therefore $\Lambda_{el} \approx L_0/A$ is nearly constant [2]. However, in TM nitrides and carbides, $\rho_0 + B$ is often large due to the high concentrations of point defects (e.g., oxygen and carbon impurities and nitrogen vacancies) [5,16]. Thus the WF law predicts that Λ_{el} should increase with increasing T at elevated temperatures [Fig. 1(a)].

Due primarily to strong covalent bonds [27], VN exhibits high melting temperature (2050 °C), hardness (15.9 GPa), electrical conductivity (33 $\mu\Omega$ cm), and chemical stability [27–29]. As a consequence, VN films have been employed to enhance the properties of cutting and grinding tools, hard electrical contacts, cylinder linings, diffusion barriers, and rechargeable microbatteries and supercapacitors [24,30–34]. A better knowledge of VN thermal and electrical transport properties could improve materials design for new applications.

This work may also provide insights into the potential of TM nitride metal/semiconductor superlattices as high

*Qzheng9@illinois.edu

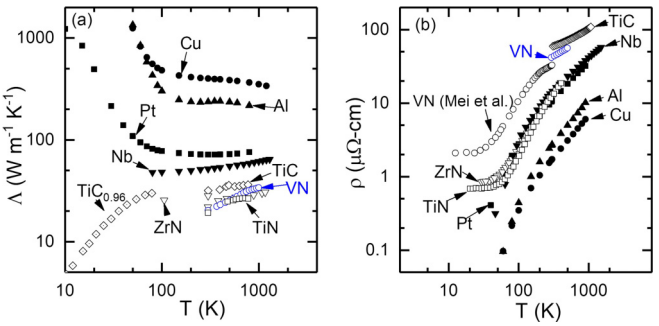

FIG. 1. (a) Temperature-dependent thermal conductivity of representative metals and transition-metal nitrides and carbides. Black symbols: Al [13], Cu [13], Pt [13], Nb [14], TiC (bulk) [15,16], $TiC_{0.96}$ (bulk) [5], ZrN (bulk) [17], TiN (RT) [18], and TiN (high T) [16], Blue open circles: VN epitaxial layers measured in this work. (b) Temperature-dependent electrical resistivity of representative metals and transition-metal nitride and carbide. Black symbols: Al [13], Cu [13], Pt [13], Nb [19], TiC [20], ZrN (bulk) [21], TiN (thin film) [22], and VN (thin film) [23]. Blue open circles: VN epitaxial layers measured in this work.

temperature materials for thermoelectric energy conversion. In our early work on (Zr,W)N/ScN superlattices, we attributed the minimum in the cross-plane thermal conductivity as a function of superlattice period to the intermixing of interfaces while a more recent work on $TiN/Al_{0.72}Sc_{0.28}N$ attributed such a minimum to coherent phonon effects [35,36]. A better understanding of the lattice thermal conductivity in metallic TM nitrides could provide an important parameter for determining the efficiency of thermoelectric materials.

II. EXPERIMENT

VN_x/MgO(001) layers are grown in a load-locked ultrahigh-vacuum magnetically unbalanced dc magnetron sputter deposition system from a 7.6-cm diameter, 99.95% pure, V disk target in 20-mTorr N_2 atmospheres as described in Ref. [37]. Film N/V ratios, determined by Rutherford backscattering spectrometry (RBS), are varied from 1.00 ± 0.05 to 0.76 ± 0.05 by increasing the growth temperature from 430 to 740 °C. The combination of x-ray diffraction ω-2θ and ϕ scans with selected-area electron diffraction and high-resolution cross-sectional transmission electron microscopy analyses demonstrate that the VN_x films are NaCl-structure epitaxial single crystals which grow cube-on-cube $(001)_{VNx}||(001)_{MgO}$ and $[100]_{VNx}||[100]_{MgO}$ with respect to the substrate [38]. Figure 2(a) is a representative cross-sectional scanning transmission electron micrograph acquired near a VN/MgO(001) film-substrate interface along the [010] zone axis. The image contrast scales primarily with the square of the average atomic number down the electron column; as a result, the film, which contains V ($Z = 23$), appears lighter than the substrate for which the element with the highest Z value is Mg ($Z = 12$). The single-crystalline nature of the film is demonstrated by well-ordered VN lattice fringes, observed to be registered cube-on-cube with respect to MgO. Spectral density plots produced from intensity line profiles extracted parallel to the interface in the film and substrate regions [as shown Fig. 2(a)] are plotted in Fig. 2(b). The curves are reminiscent of diffraction patterns calculated using the kinematical approximation, with peaks at 4.14 and 4.21 Å corresponding to the in-plane lattice parameters of VN and MgO. That the peaks occur at different distances indicates the film is not fully strained, consistent with high-resolution reciprocal lattice mapping analyses, see below.

Out-of-plane ($a_\perp$) and in-plane ($a_{||}$) lattice parameters of the epitaxial VN_x(001) films are obtained from high-resolution reciprocal lattice maps (HR-RLM) around symmetric 002 and asymmetric 113 reflections. Figures 2(c) and 2(d) show representative HR-RLMs, acquired using Cu $K\alpha$ radiation, around the 002 and 113 reflections of the stoichiometric VN/MgO(001) plotted as logarithmic isointensity contours as a function of in-plane Q_x and out-of-plane Q_z reciprocal-lattice vectors. The relaxed lattice parameters a_0 of VN_x epitaxial layers are determined from $a_\perp$ and $a_{||}$ through the relationship $a_0 = a_\perp(1 - \frac{2\nu(a_\perp - a_\parallel)}{a_\parallel(1+\nu)})$ in which the Poisson ratio $\nu = 0.23$ is derived in our previous work on epitaxial VN/MgO(001) [38]. a_0 decreases from 4.14 Å at $x = 1.00$ to 4.09 Å at $x = 0.76$ (see Table I), in good agreement with previous studies of bulk and sputter-deposited VN_x [38–41]. VN(001) in-plane $\xi_\parallel$ and out-of-plane $\xi_\perp$ x-ray coherence lengths, which serve as measures of crystalline quality, are obtained from the width of symmetric 002 reflections parallel Q_x and perpendicular Q_z to the diffraction vector $\mathbf{k}$ through the relationships: $\xi_\parallel = 2\pi/|\Delta Q_x|$ and $\xi_\perp = 2\pi/|\Delta Q_z|$ [42]. From the results shown in Fig. 2, $\xi_\parallel = 23$ nm and $\xi_\perp = 44$ nm. $\xi_\perp$ values depend, in addition to structural quality [23], on film thickness [23,42]. Stoichiometric epitaxial Group-IVB TM nitrides TiN/MgO(001), ZrN/MgO(001), and HfN/MgO(001), grown under conditions similar to those of the present Group-VB VN(001) layers, exhibit $\xi_\parallel$ values of 86 [21,43] 18 [21], and 22 nm [44], respectively.

The thicknesses of the VN_x epitaxial layers are determined using RBS atomic areal density and HR-RLM lattice parameters to within ±5%. For the five samples measured, the thickness varies from 160 to 229 nm (see Table I). The thickness of the stoichiometric VN sample is 192 nm, which is close to the value of 194 nm obtained using picosecond acoustics with the previously reported longitudinal sound velocity $v_{001} = 9.8\,\mathrm{km\,s^{-1}}$ [38]. The complex index of refraction of VN is $n \approx 1.49 + 3.44i$ at 785 nm as measured by ellipsometry, corresponding to an optical absorption depth of $\alpha^{-1} = \frac{\lambda}{4\pi k} = 18$ nm, consistent with recent results on the optical properties of VN_x/MgO(001) [37].

A modified time-domain thermoreflectance (TDTR) method, which required no additional transducer layer to be deposited on the sample surface, is used to measure the thermal conductivity of epitaxial VN_x thin films [45,46]. In our TDTR measurement, a train of optical pulses at a repetition rate of 80 MHz, generated by a mode-locked Ti:sapphire laser at a wavelength of 785 nm, is split into separate pump and probe beams with the optical path of the pump beam controlled by a mechanical delay stage. The pump beam is modulated at a frequency of 4.1 MHz by an electro-optical modulator. This frequency is lower than the typical 10 MHz modulation used in our previous TDTR studies and is chosen to enhance the sensitivity to VN thermal conductivity (see Fig. 4). The pump

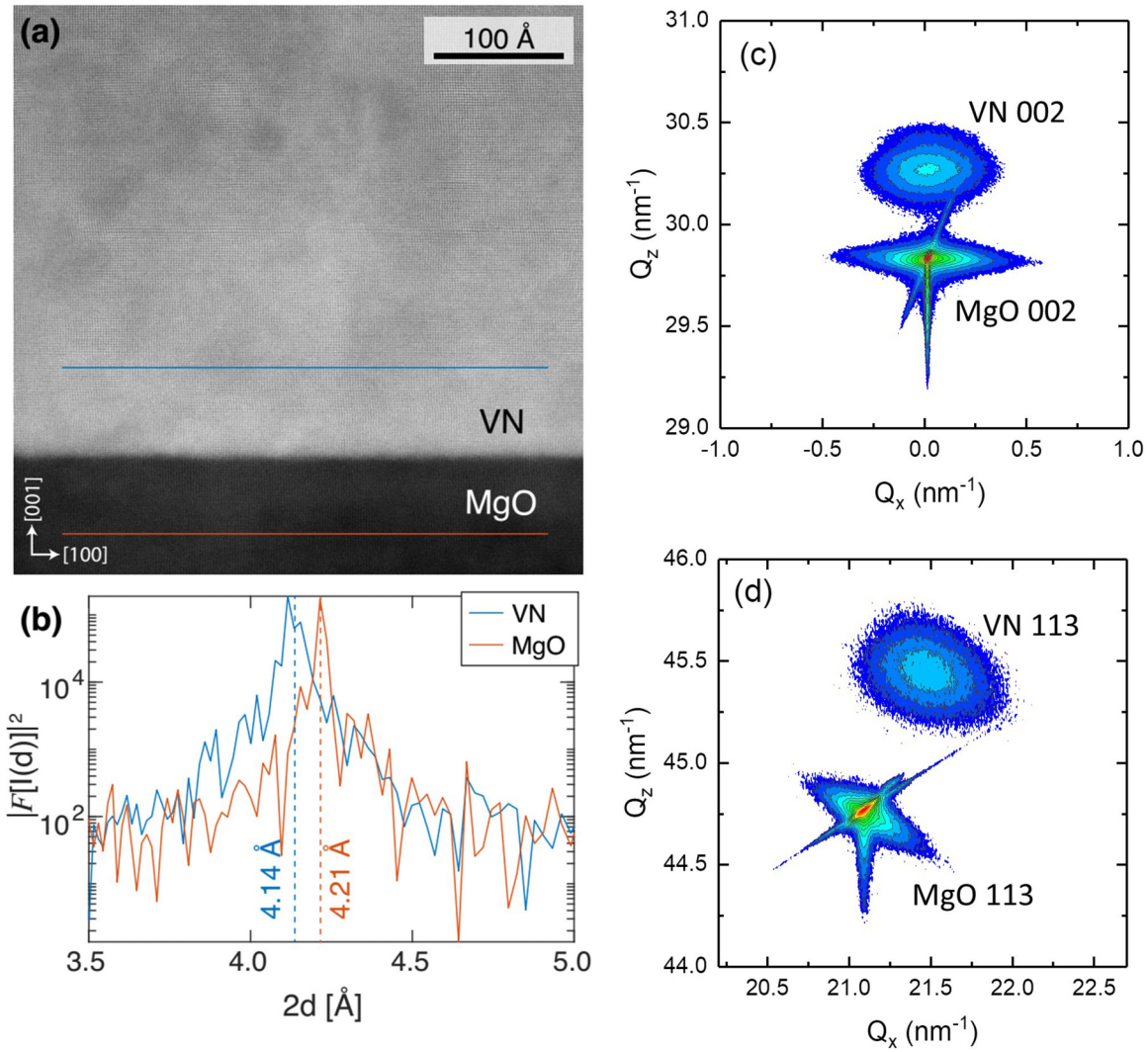

FIG. 2. (a) Cross-sectional scanning transmission electron micrograph acquired near the 192-nm-thick VN/MgO(001) film-substrate interface along the [010] zone axis. (b) Spectral density plots produced from intensity line profiles extracted parallel to the interface in the film and substrate regions along the blue (VN) and orange (MgO) lines, respectively. The abscissa in (b) is doubled to account for the two atomic columns per conventional NaCl-structure unit cells along the [010] projection. (c) and (d) High-resolution reciprocal-lattice maps, acquired with Cu $K\alpha$ radiation, about the symmetric 002 and asymmetric 113 reflection from stoichiometric VN/MgO(001) in (a).

and probe beams are focused on the sample through a 5× objective lens to a $1/e^2$ intensity radius of ≈10.7 μm. The total beam power of 15 mW creates a steady-state temperature rise of ≈4 K at room temperature and 8 K at 1000 K. The changes in the intensity of the reflected probe beam created by the pump beam are measured using phase-sensitive lock-in detection. The ratio of the in-phase (V_{in}) and out-of-phase (V_{out}) signals from the lock-in amplifier is then fit to a thermal

TABLE I. Composition x, growth temperature T, areal density, relaxed lattice constant a_0, film thickness h, mass density ρ, and longitudinal sound velocity v_{001} of epitaxial VN_x samples.

		Areal density of atom (10^{18} cm^{-2})					
x	T (°C)	V	N	a_0 (Å)	h (nm)	ρ(g cm^{-3})	v_{001}(km s^{-1})
1.00	430	1.08	1.08	4.14	192	6.06	9.8
0.93	509	1.15	1.07	4.13	195	6.04	9.3
0.88	589	1.28	1.12	4.11	209	6.04	8.0
0.84	636	1.44	1.21	4.10	229	6.03	7.3
0.76	740	1.06	0.81	4.09	160	5.98	7.3

diffusion model obtained from an analytical solution for heat flow in a layered structure [45]. Based on the measured film thickness and the picosecond acoustic signal from TDTR [38], we also derived the longitudinal speed of sound v_{001} in the five VN_x samples to a precision of $\pm 0.4\,\mathrm{km\,s^{-1}}$ (Table I).

In a conventional TDTR measurement, the sample is coated with a 60–90 nm metal transducer which provides the thermoreflectance signal. At the beginning of these studies, we tried using Pt as the transducer layer. However, a dramatic change in the interface thermal conductance between Pt and VN_x was observed at $T > 700$ K. We tentatively attribute this observation to reduction of the native oxide at the Pt/VN_x interface by the VN_x layer. This uncontrolled change in interface conductance often led to inconsistent measurements. Therefore, we instead studied bare VN_x films without an additional transducer layer. The room-temperature thermoreflectance dR/dT of VN_x is $2.2 \times 10^{-5}\,\mathrm{K^{-1}}$ at 785 nm, significantly smaller than for Al or TiN, but still sufficient for TDTR measurements [47,48].

Temperature-dependent VN_x TDTR measurements from 300–1000 K are performed by mounting the VN_x/MgO(001) specimen on a heater stage in a vacuum chamber and monitoring the sample temperature with a Pt resistance thermometer. To minimize sample oxidation, the chamber is pumped with a turbomolecular pump to maintain a pressure lower than 7.5×10^{-4} Torr at high temperature. The electrical resistivity ρ of the VN_x films is measured from 300 to 500 K by the Van der Pauw method using a heating stage in ambient air. To confirm the reliability of the data measured in ambient, we also performed Van der Pauw method resistivity measurements of the $VN_{0.84}$ sample from 300 to 920 K using a high vacuum furnace in a vacuum better than 5×10^{-7} Torr. The resistivity vs temperature from 300 to 500 K obtained from the two facilities agrees to within 1%. The lateral dimensions of the other samples are too small to be measured with the high vacuum system.

III. RESULTS AND DISCUSSION

Representative TDTR data and model fitting for a 192-nm-thick stoichiometric VN sample measured at 300 and 1000 K are shown in Fig. 3. The thermal transport model used for fitting includes parameters for the thermal conductivity, heat capacity, and thickness of the VN_x layers, and the MgO substrate, the thermal conductance of the VN_x/MgO interface, and the thicknesses of the optical absorption layer [45]. In TDTR data analysis, the thermal conductivity of the VN_x layer and thickness of the optical absorption layer are used as free parameters for fitting. The thickness of the VN_x layer is measured by RBS. The MgO substrate thickness of 0.5 mm is essentially semi-infinite for our TDTR measurements at 4.1 MHz modulation frequency [49]. The VN_x/MgO interface thermal conductance is measured separately on a sample specifically designed to optimize that measurement (see below). The thermal conductivity and heat capacity of the single-crystal MgO(001) substrate and the temperature- and composition-dependent heat capacity of VN_x are taken from Refs. [50–52]. The reference volumetric heat capacity of stoichiometric VN at its Debye temperature of 800 K (see below) is $4.72\,\mathrm{J\,cm^{-3}\,K^{-1}}$ [52], in good agreement with the

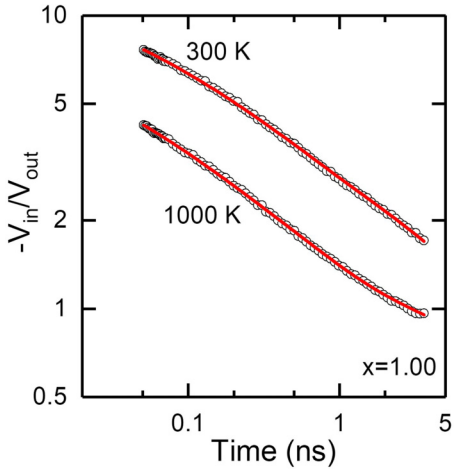

FIG. 3. Example TDTR data: $-V_{in}/V_{out}$ vs delay time (open circles) for the 192-nm-thick epitaxial stoichiometric VN/MgO(001) film measured at 300 and 1000 K. Data (black open circles) are compared to the predictions of the thermal transport model described in the text (red solid lines) with the optical absorption length and the thermal conductivity of the VN layer as free parameters.

Dulong Petit value of $3Nk_B \approx 4.67\,\mathrm{J\,cm^{-3}\,K^{-1}}$ calculated using the measured lattice constants at room temperature and the thermal expansion coefficient from the literature [39,52]. At 300 K, the VN volumetric heat capacity from the reference is $3.58\,\mathrm{J\,cm^{-3}\,K^{-1}}$. We also measured the thermal conductivity of the same MgO substrate used for VN_x growth by conventional TDTR with an 80-nm Al coating. The measured MgO thermal conductivity results from 300 to 600 K agree with reference data to within 5% [51].

We define the sensitivity of the fit S_α as the logarithmic derivative $-V_{in}/V_{out}$ with respect to each of the parameters α in order to gauge how each parameter influences the output of the model. The larger the value of S_Λ, the smaller the error propagated from the other parameters into the measured thermal conductivity.

Figures 4(a) and 4(b) show the sensitivity of the fits in Fig. 3 to changes in the various parameters in the thermal-transport

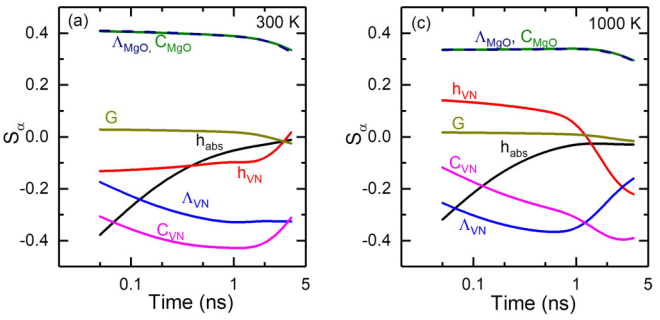

FIG. 4. Calculated sensitivity parameters in TDTR measurements as a function of delay time at (a) 300 K and (b) 1000 K for important parameters used in modeling 192-nm-thick VN/MgO: VN thermal conductivity and heat capacity (Λ_{VN} and C_{VN}), absorption layer thickness and VN thickness (h_{abs} and h_{VN}), VN/MgO interface thermal conductance (G), and MgO substrate thermal conductivity and heat capacity (Λ_{MgO} and C_{MgO}).

model for VN_x/MgO. TDTR measurements of thick VN_x films have moderate sensitivity to Λ_{VN} (0.25–0.4) because the thermal resistance for heat transport through the thickness of the VN_x film is larger than the thermal resistance of the VN_x/MgO interface, i.e., $h/\Lambda_{VN} > G^{-1}$. The measurement sensitivity to interfacial thermal conductance G is small ($|S_G| < 0.05$) so long as G is large ($>0.7\,\mathrm{GW\,m^{-2}\,K^{-1}}$). This limits the error propagation from our estimate for G: a 20% error in G propagates into only an ≈3% error in VN_x thermal conductivity. With increasing temperature from 300 to 1000 K, the thermal diffusivity of the VN layer $D = \frac{\Lambda_{VN}}{C_{VN}}$ increases by ≈20%, while the effusivity of MgO substrate $\varepsilon = \sqrt{\Lambda C}$ decreases by ≈30%. These changes in thermal properties produce pronounced variations with temperature in the TDTR signal sensitivity to the VN thickness.

Since the thickness of the absorption layer h_{abs} and the thermal conductivity of VN_x, the two free parameters in the model fitting, have maxima in their sensitivity at short (<300 ps) and long (>1 ns) time delays, respectively, we could obtain their values relatively independently. The TDTR measurement of the absorption layer thickness is 18 ± 3 nm for all VN_x samples at all temperatures, e.g., h_{abs} obtained in Fig. 3 is 18 nm at 300 K and 20 nm at 1000 K. This result agrees with the room temperature ellipsometry measurement of the imaginary part of the refractive index for VN_x of varied compositions [37]. To independently measure the thermal conductance of the VN_x/MgO interface (G), we prepared a thinner 29-nm-thick VN/MgO(001) sample that enables higher sensitivity to G. We coated this sample with an 80-nm-thick layer of Al by magnetron sputtering to avoid artifacts that are sometimes encountered in TDTR studies of semitransparent layers. By annealing the Al/VN/MgO sample overnight at 750 K in air, we obtained a metallic contact between Al/VN, presumably due to the reduction of the native oxide at the Al and VN interface by the VN layer, i.e., we hypothesize that oxygen at the Al/VN interfaces diffuses into the bulk of the VN film during annealing. The Al/VN and VN/MgO interface thermal conductances are measured to be ≈1.1 ± 0.3 and ≈0.8 ± 0.2 $\mathrm{GW\,m^{-2}\,K^{-1}}$, respectively. The thermal conductances of the two interfaces are both weakly temperature dependent from 300 to 700 K. The value of $G_{VN/MgO}$ is close to that of epitaxial TiN/MgO(001), $G \approx 0.7\,\mathrm{GW\,m^{-2}\,K^{-1}}$ at room temperature [48]. Although the diffusion of surface oxide changes the interface thermal conductance, we do not expect the oxygen diffusion into bulk VN_x to significantly affect the thermal and electrical conductivity measurements using bare VN_x. Variations in the thermal conductivity and absorption layer thickness of VN_x samples in three repeated TDTR measurements are less than 4%, smaller than the measurement uncertainty. The electrical resistivity of $VN_{0.84}$ measured in a high-vacuum system after the TDTR measurement to 1000 K also shows good agreement with the resistivity results between 300 and 500 K obtained earlier [see Fig. 6(a)]. A vanadium oxide layer of 1 to 3 nm corresponds to an oxygen areal density of $\sim 10^{16}\,\mathrm{cm^{-2}}$ [53]. Even if all the oxygen from the surface diffuses into the bulk, it will result in ∼1 at. % concentration of extra oxygen in the VN_x layer. Assuming the effect of the 1 at. % oxygen is similar to 1 at. % N vacancies in VN_x, the change in electrical and thermal conductivity should be below experimental uncertainty, consistent with what we observed.

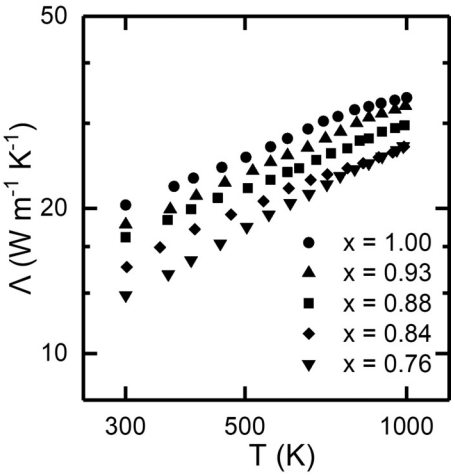

FIG. 5. Thermal conductivity of VN_x ($x = 0.76, 0.84, 0.88, 0.93$, and 1.00) as a function of temperature.

We plot data for the thermal conductivity of VN_x as a function of temperature and composition x in Fig. 5. The thermal conductivities increase monotonically over the temperature range $300 < T < 1000$ K and decrease with increasing N vacancy concentration. The temperature dependence of the thermal conductivity becomes slightly stronger with decreasing x. Over this temperature range, Λ increases by a factor of 2 for $x = 0.76$, and increases by a factor of 1.7 for $x = 1.00$.

In Fig. 6(a) we plot our measurements of the electrical resistivity ρ of VN_x as a function of temperature. The VN_x(001) room-temperature resistivity $\rho_{300\,K}$ increases from 42 to 73 $\mu\Omega\,$cm as x decreases from 1.00 to 0.76. The data for stoichiometric VN(001) are larger than the reported $\rho_{300\,K}$ value of 33 $\mu\Omega\,$cm for VN/MgO(011) [23]. This larger resistivity suggests that the VN(001) sample may be slightly off-stoichiometry or contaminated by a small amount of carbon or oxygen that is not detectable in the RBS measurements. The electrical resistivity of $VN_{0.84}$ measured in a high-vacuum furnace shows a linear behavior up to 920 K, consistent with the measurement from 300 to 500 K, which justifies the linear extrapolation of the data of lower temperature measurements. Such behavior is different from the temperature-dependent resistivity in a previous report on $VN_{0.92}$ powder with 8 at % oxygen which displayed an irreproducible anomaly at ∼720 K due to the electrically active oxygen [55].

The resistivity ρ increases with temperature due to the increasing strength of electron-phonon scattering. The temperature coefficient of resistivity (TCR) over this temperature range, defined as $(\rho_{500\,K} - \rho_{300\,K})/\Delta T$, increases from 3.6×10^{-8} to $6.9 \times 10^{-8}\,\Omega\,\mathrm{cm\,K^{-1}}$ as x increases from 0.76 to 1.00.

We calculated the Debye temperature Θ_D using Houston's method [56] and the elastic constants measured in our previous work on stoichiometric VN [38], $\Theta_D \approx 800$ K. The longitudinal elastic constant decreases with decreasing x (see Table I). If we assume that all three independent elastic constants of VN_x have the same dependence on x, then $700 < \Theta_D < 800$ K for $0.76 < x < 1.0$. The scaled temperatures in our work are therefore $0.4 < \frac{T}{\Theta_D} < 1.4$.

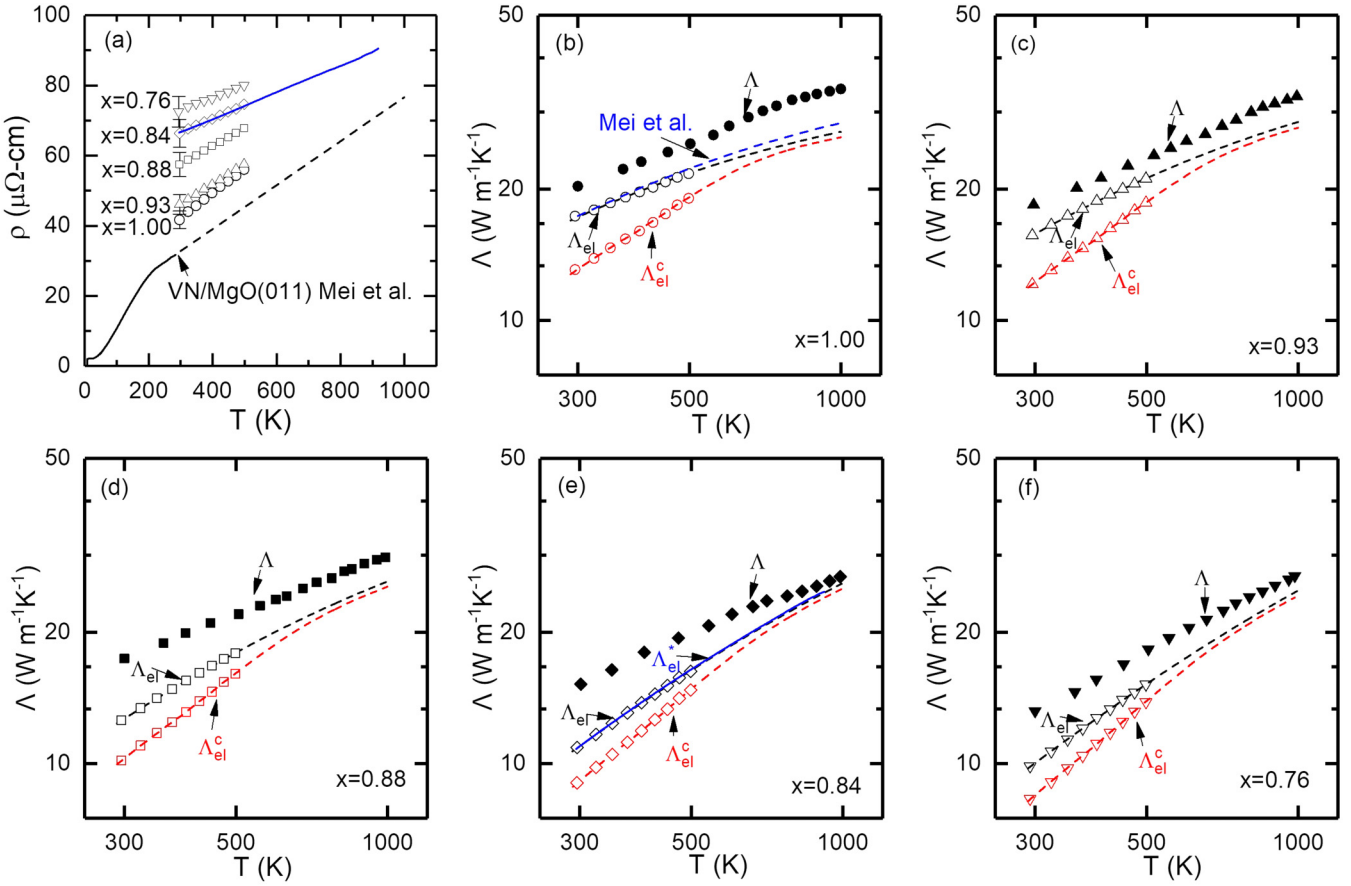

FIG. 6. (a) Electrical resistivity of VN_x/MgO(001) layers as a function of temperature measured in ambient air (open symbols) and high vacuum (blue line). Previously published data for a stoichiometric epitaxial VN/MgO(011) film deposited by the same method (solid line) together with a linear extrapolation of this data (dashed line) are included for comparison [23]. The blue line is the result for $VN_{0.84}$ measured with a different Van der Pauw four-point probe system in a high-vacuum furnace as described in the text. (b)–(f) The same thermal conductivity of VN_x films as in Fig. 5 (filled black symbols) and their electronic thermal conductivity calculated from corresponding electrical resistivity by the WF law with a constant Lorenz number $L = L_0$ (black open symbols = Λ_{el}) and $L = L(T)$(red open symbols = Λ^c_{el} from Eq. (6)) [54] as a function of temperature from 300 to 1000 K. The black and red dashed lines are Λ_{el} and Λ^c_{el} calculated via the WF law with $L = L_0$ and $L = L(T)$ obtained from a linear extrapolation of the electrical resistivity data (open symbols) from 300 to 500 K. Λ_{el} calculated from $\rho(T)$ with the same 300 K resistivity as the stoichiometric VN sample and the TCR for epitaxial VN at 250–300 K in previous work [23] is also included in (b) (blue dashed line). The blue solid line in (e) shows the converted Λ_{el} values for $VN_{0.84}$ from the direct high vacuum measurement result in (a) (blue line) from 300 to 920 K.

To understand the temperature-dependent behavior of Λ, we first apply the WF law with a constant Lorenz number

$$\Lambda_{el}(T) \approx \frac{L_0 T}{\rho}, \tag{2}$$

in which L_0 is the Sommerfeld value of Lorenz number $L_0 = 2.44 \times 10^{-8}\,\Omega\,\mathrm{W\,K^{-2}}$. $\Lambda_{el}(T)$ results from Eq. (2) for each VN_x sample are compared to the total thermal conductivities measured by TDTR in Figs. 6(b)–6(f). We conclude that the thermal conductivity of VN_x between 300 and 1000 K is predominantly electronic in origin.

An empirical relationship between the electrical resistivity ρ and thermal conductivity Λ of metal alloys was suggested by Smith and Palmer and is often used to predict the thermal conductivity of alloys from measurements of the electrical resistivity [57]

$$\Lambda = \frac{C L_0 T}{\rho} + \Lambda_L, \tag{3}$$

in which CL_0 is the effective Lorenz number and Λ_L is the lattice thermal conductivity; C and Λ_L are free parameters that are adjusted to fit the data. The Smith-Palmer equation is often a good description of the thermal conductivity of alloys, although significant deviations were observed by us in some Ni solid solutions [58]. Furthermore, application of the Smith-Palmer equation assumes that the Lorenz number does not depend strongly on temperature or alloy composition and that the lattice thermal conductivity does not depend on composition [58]. Nevertheless, we expect that the Smith-Palmer plot shown in Fig. 7 provides a useful first estimate of the Lorenz number and lattice thermal conductivity. The linear fit of Fig. 6 gives $C = 0.90$ and $\Lambda_L = 5\,\mathrm{W\,m^{-1}\,K^{-1}}$.

At the next level of sophistication, we consider the temperature dependence of the Lorenz number L. With the assumptions of spherical Fermi surfaces, equilibrium phonon distributions, a Debye phonon spectrum, and the predominance of normal processes for electron-phonon scattering [2,59], the theoretical expression for the Lorenz ratio $L_{\rm th}(T)/L_0$ as a function of temperature is [1,60]

$$\frac{L_{\rm th}(T)}{L_0} = \frac{\rho_{\rm imp}/A + \left(\frac{T}{\Theta_D}\right)^5 J_5\left(\frac{\Theta_D}{T}\right)}{\rho_{\rm imp}/A + \left(\frac{T}{\Theta_D}\right)^5 J_5\left(\frac{\Theta_D}{T}\right)\left[1 + \frac{3}{\pi^2}\left(\frac{k_F}{q_D}\right)^2\left(\frac{\Theta_D}{T}\right)^2 - \frac{1}{2\pi^2}\frac{J_7\left(\frac{\Theta_D}{T}\right)}{J_5\left(\frac{\Theta_D}{T}\right)}\right]}. \quad (4)$$

Here k_F is the Fermi wave vector, and Θ_D and q_D are the Debye temperature and Debye wave vector, respectively. The Debye integrals J_n are defined as

$$J_n\left(\frac{\Theta_D}{T}\right) = \int_0^{\Theta_D/T} \frac{x^n e^x}{(e^x-1)^2} dx. \quad (5)$$

Equation (4) has been used to understand the electronic thermal transport in metals and alloys [3,59]. The second term in the bracket of the denominator involving k_F/q_D is due to electron-phonon inelastic small-angle scattering (vertical processes). The third term in the bracket is a correction that accounts for situations where large-angle scattering can reverse the electron direction without restoring the distribution back to equilibrium [59]. Electron-impurity scattering is included as $\rho_{\rm imp}/A$ in the equation.

In Fig. 8 we plot the Lorenz ratio as a function of reduced temperature as predicted by Eq. (4) and give comparisons to experimental results for several metals. The similarity of the Lorenz ratios for Cu, Ta, Nb, and ThN is striking [3,54,61]. Here the red line shows $L_{\rm th}(T)/L_0$ for an ideal free-electron-like monovalent metal where $k_F/q_D = 2^{-1/3}$. The drop in $L_{\rm th}(T)$ when the temperature is decreased below Θ_D is caused by the dominance of inelastic vertical scattering of electrons by phonons. At high temperature, the greater probability of large-angle quasielastic scattering between electrons and high energy phonons reduces the deviation between $L(T)$ and L_0. A higher level of impurity (large $\rho_{\rm imp}/A$) results in a stronger elastic scattering of electron, reducing the deviation of $L_{\rm th}(T)$ from the Sommerfeld value. Impurity scattering dominates at low temperature when electron-phonon scattering is weak.

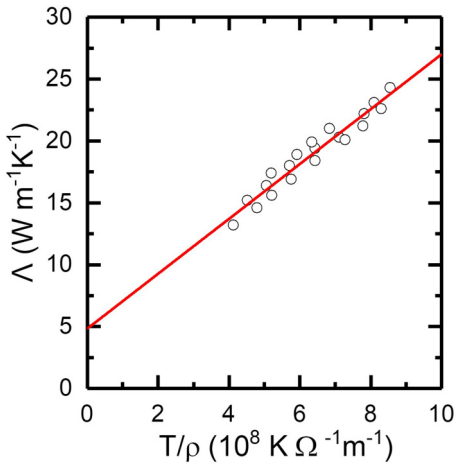

FIG. 7. Smith-Palmer plot, see Eq. (3), for VN_x from 300 to 500 K.

Due to the lack of detailed knowledge about the electron-phonon coupling constant, Fermi wave vector, and residual resistance of our samples, a direct calculation of $L_{\rm th}(T)$ for VN_x using Eq. (4) is not possible. Considering the relatively small difference among $L(T)$ values for normal metals shown in Fig. 8, we approximate the Lorenz function of VN_x with $L(T)$ interpolated from a similar NaCl-structure TM nitride ThN scaled by the relative Debye temperatures. ThN also shows an increasing thermal conductivity with increasing temperature over a similar range of scaled temperature [54].

Since static point defects typically elastically scatter electrons of different energy with equal effectiveness, the WF law with $L(T) = L_0$ is usually valid for the residual resistivity due to point-defect scattering. Assuming negligible deviation from Matthiessen's rule, i.e., different scattering processes are independent of each other [62], an improved model by adding the thermal resistance from electron-phonon and electron-defect scattering based on the temperature-dependent Lorenz function follows as [6,61]

$$\Lambda_{\rm el}^c = \left(\frac{\rho_i}{L(T)T} + \frac{\rho(x)-\rho_i}{L_0 T}\right)^{-1}. \quad (6)$$

ρ_i is the electrical resistivity of defect-free VN which is derived from subtracting the 9 $\mu\Omega$ cm difference in $\rho_{300\,\rm K}$ between the stoichiometric VN in our previous work [23] and the VN in this work and the 2 $\mu\Omega$ cm residual resistivity of VN in Ref. [23] from the ρ of the stoichiometric VN. $\rho(x)$ is the resistivity of VN_x with N vacancies.

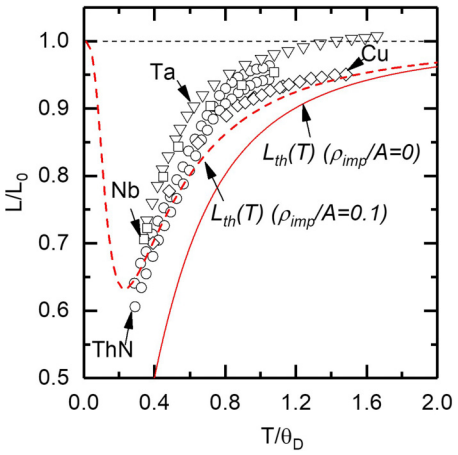

FIG. 8. Temperature variation of the Lorenz function normalized to the Sommerfeld value from experiments and theory as a function of reduced temperature for Cu [3,61], Ta [61], Nb [61], and ThN [54]. Lorenz function $L_{\rm th}(T)$ calculated from Eq. (4) where $k_F/q_D = 2^{-1/3}$ assuming the impurity term $\rho_{\rm imp}/A = 0$ (red solid line) and $\rho_{\rm imp}/A = 0.1$ (red dashed line) are also included for comparison.

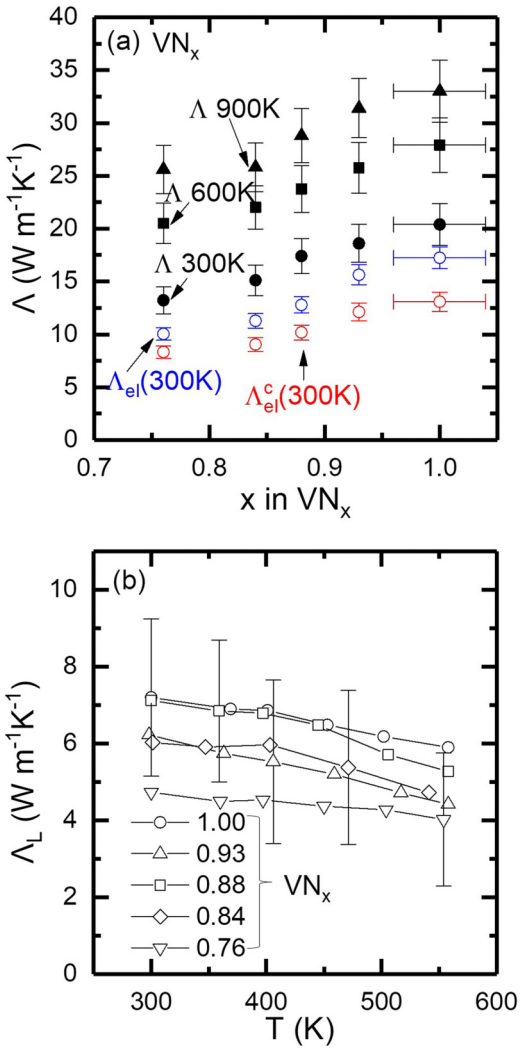

FIG. 9. (a) Thermal conductivity (Λ, black filled symbols) of VN_x films as a function of composition x at representative temperatures and 300 K electronic thermal conductivity with constant Lorenz number $L = L_0$ (black open symbols $= \Lambda_{el}$) and $L = L(T)$ [red open symbols $= \Lambda^c_{el}$ from Eq. (6)] [54]. (b) Lattice thermal conductivity Λ_L as a function of temperature and composition derived from $\Lambda_L = (\Lambda - \Lambda^c_{el})$.

Applying Eq. (6) to VN_x, we obtain the corrected electronic thermal conductivity Λ^c_{el} as a function of temperature. As shown in Figs. 6(b)–6(f), Λ^c_{el} is 20%–30% smaller at 300 K than Λ_{el} calculated with L_0 and approaches Λ_{el} at high temperature. As the concentration of nitrogen vacancies increases, i.e., as x decreases, the difference between Λ^c_{el} and Λ_{el} decreases because the elastic scattering of electrons by defects becomes stronger, hence the contribution from the second term in Eq. (6) becomes larger.

In Fig. 9(a) we plot the total thermal conductivity Λ and our two calculations of the electronic component Λ_{el} and Λ^c_{el} for VN_x as a function of composition at three temperatures. The total and electronic thermal conductivities decrease as the vacancy concentration increases, and tends to flatten out at high vacancy concentration, a behavior similar to what has been observed in other TM carbides and nitrides [24].

We plot the VN_x lattice thermal conductivity derived by subtracting the electronic component $\Lambda_L = (\Lambda - \Lambda^c_{el})$ in Fig. 9(b). For all samples, Λ_L constitutes approximately 35%–40% of the total thermal conductivity at 300 K and decreases as temperature increases, contributing 20%–25% to the total thermal conductivity at 500 K. Λ_L values derived this way are approximately 20%–30% smaller than those derived from the WF law with the Sommerfeld Lorenz number at 300 K and are comparable to the lattice thermal conductivity of closely related materials, such as ThN and TaC, at high temperature [5,24]. However, Λ_L is still small compared to estimates of the lattice thermal conductivity of TiC and ZrN in the intermediate and high temperature ranges [6,24,35]. We attribute this to relatively stronger electron-phonon scattering in VN and the significant contribution of phonon scattering by N vacancies.

Λ_L in VN_x does not show a $\Lambda_L \propto 1/T$ relation characteristic of anharmonic three phonon interactions [see Fig. 9(b)]. In Makinson's transport theory for metals [1], the lattice thermal conductivity obtained from electron-phonon scattering alone should be nearly independent of temperature at $T > 0.6\Theta_D$. For the temperature range of our measurements [$0.4 < \frac{T}{\Theta_D} < 0.7$ in Fig 9(b)] the weak temperature dependence of Λ_L indicates that the thermal resistance from electron-phonon scattering is of the same order as the thermal resistance from anharmonic phonon interactions.

As seen in Fig. 9(b), when the vacancy concentration increases, the lattice thermal conductivity Λ_L decreases and has a weaker dependence on temperature. In the high-temperature limit of a Debye model with the assumption of phonon scattering rates that scale quadratically with phonon frequency, the lattice thermal conductivity limited by point-defect scattering is

$$\Lambda^p_L = \Lambda^i_L \frac{\omega_0}{\omega_D} \tan^{-1}\left(\frac{\omega_D}{\omega_0}\right). \quad (7)$$

Λ^i_L is the lattice thermal conductivity of intrinsic phonon scattering, ω_D is the Debye frequency, and ω_0 is a characteristic frequency at which the phonon point-defect scattering rate is equal to the phonon-phonon scattering rate [3,63]. Equation (7) predicts $\Lambda^p_L \propto T^{-1/2}\varepsilon^{-1/2}$ when point-defect scattering is strong and $\Lambda^p_L \propto \varepsilon^{-1}$ when point-defect scattering is weak, in which ε is proportional to the point-defect concentration [63,64]. Therefore, Λ^p_L is expected to become smaller as the vacancy concentration increases and should have a weaker temperature dependence than Λ^i_L. We also note that the longitudinal sound velocity in VN_x decreases with increasing vacancy concentration (see Table I) which reduces the velocity of acoustic phonons. This lattice softening with decreasing x may also contribute to the trend of decreasing lattice thermal conductivity with decreasing x.

IV. CONCLUSIONS

In summary, we measured the temperature-dependent thermal conductivity from 300 to 1000 K of epitaxial VN_x/MgO(001) ($0.76 < x < 1.00$) thin films by TDTR and compared the result with the electronic thermal conductivity calculated from the Wiedemann-Franz law. The increase in the thermal conductivity in the temperature range of our measurement is predominantly electronic in origin. The relatively

low lattice thermal conductivity and its weak temperature dependence are attributed to strong electron-phonon coupling in VN_x. Increasing vacancy concentration was found to reduce both the electron and lattice thermal conductivities and lead to weaker temperature dependence for the lattice contribution to the thermal conductivity.

ACKNOWLEDGMENTS

Experimental characterization was carried out in the Frederick Seitz Materials Research Laboratory (MRL) at the University of Illinois. Q.Z. gratefully thank the help from Professor Leslie H. Allen's group on the measurement of the electrical resistivity in the high vacuum system. We kindly acknowledge financial support from the Swedish Research Council (VR) Project Grants 2009-00971, 2013-4018, and 2014-5790, and the Swedish Government Strategic Research Area Grant in Materials Science (SFO Mat-LiU) on Advanced Functional Materials. D.G.S. gratefully acknowledges financial support from the Olle Engkvist Foundation and access to supercomputer resources provided by the Swedish National Infrastructure for Computing (SNIC).

[1] R. E. B. Makinson, Math. Proc. Cambridge Philos. Soc. **34**, 474 (1938).
[2] J. M. Ziman, *Electrons and Phonons: The Theory of Transport Phenomena in Solids* (Oxford University Press, Oxford, 1960), p. 322.
[3] P. G. Klemens and R. K. Williams, Int. Met. Rev. **31**, 197 (1986).
[4] A. Jain and A. J. H. McGaughey, Phys. Rev. B **93**, 081206 (2016).
[5] L. G. Radosevich and W. S. Williams, Phys. Rev. **181**, 1110 (1969).
[6] W. H. Butler and R. K. Williams, Phys. Rev. B **18**, 6483 (1978).
[7] W. Weber, Phys. Rev. B **8**, 5093 (1973).
[8] S. J. Poon and T. H. Geballe, Phys. Rev. B **18**, 233 (1978).
[9] P. B. Allen, Phys. Rev. Lett. **59**, 1460 (1987).
[10] A. B. Mei, A. Rockett, L. Hultman, I. Petrov, and J. E. Greene, J. Appl. Phys. **114**, 193708 (2013).
[11] E. I. Isaev, S. I. Simak, I. A. Abrikosov, R. Ahuja, Y. K. Vekilov, M. I. Katsnelson, A. I. Lichtenstein, and B. Johansson, J. Appl. Phys. **101**, 123519 (2007).
[12] Z. Lin, L. V. Zhigilei, and V. Celli, Phys. Rev. B **77**, 075133 (2008).
[13] W. M. Haynes, *CRC Handbook of Chemistry and Physics*, 96th ed. (CRC, Boca Raton, FL, 2015).
[14] J. P. Moore, R. S. Graves, and R. K. Williams (unpublished).
[15] D. G. Cahill, S. M. Lee, and T. r. I. Selinder, J. Appl. Phys. **83**, 5783 (1998).
[16] R. E. Taylor and J. Morreale, J. Am. Ceram. Soc. **47**, 69 (1964).
[17] J. Adachi, K. Kurosaki, M. Uno, and S. Yamanaka, J. Alloys Compd. **399**, 242 (2005).
[18] H. O. Pierson, *Handbook of Refractory Carbides & Nitrides: Properties, Characteristics, Processing and Apps* (Elsevier Science, Amsterdam, 1996).
[19] N. Tralshawala, J. F. Zasadzinski, L. Coffey, W. Gai, M. Romalis, Q. Huang, R. Vaglio, and K. E. Gray, Phys. Rev. B **51**, 3812 (1995).
[20] W. S. Williams, J. Am. Ceram. Soc. **49**, 156 (1966).
[21] A. B. Mei, B. M. Howe, C. Zhang, M. Sardela, J. N. Eckstein, L. Hultman, A. Rockett, I. Petrov, and J. E. Greene, J. Vac. Sci. Technol. A **31**, 061516 (2013).
[22] M. A. Wall, D. G. Cahill, I. Petrov, D. Gall, and J. E. Greene, Phys. Rev. B **70**, 035413 (2004).
[23] A. B. Mei *et al.*, Phys. Rev. B **91**, 054101 (2015).
[24] W. S. Williams, JOM **50**, 62 (1998).
[25] R. Franz and G. Wiedemann, Ann. Phys. **165**, 497 (1853).
[26] U. Mizutani, *Introduction to the Electron Theory of Metals* (Cambridge University Press, Cambridge, 2001).
[27] V. A. Gubanov, A. L. Ivanovsky, and V. P. Zhukov, *Electronic Structure of Refractory Carbides and Nitrides* (Cambridge University Press, Cambridge, 2005).
[28] R. Sanjinés, C. Wiemer, P. Hones, and F. Lévy, J. Appl. Phys. **83**, 1396 (1998).
[29] C. Stampfl, W. Mannstadt, R. Asahi, and A. J. Freeman, Phys. Rev. B **63**, 155106 (2001).
[30] M. B. Takeyama, T. Itoi, K. Satoh, M. Sakagami, and A. Noya, J. Vac. Sci. Technol. B **22**, 2542 (2004).
[31] X. Chu, S. A. Barnett, M. S. Wong, and W. D. Sproul, J. Vac. Sci. Technol. A **14**, 3124 (1996).
[32] L. E. Toth, *Transition Metal Carbides and Nitrides* (Academic, New York, 1971).
[33] X. Zhou, H. Chen, D. Shu, C. He, and J. Nan, J. Phys. Chem. Solids **70**, 495 (2009).
[34] Q. Sun and Z.-W. Fu, Electrochim. Acta **54**, 403 (2008).
[35] V. Rawat, Y. K. Koh, D. G. Cahill, and T. D. Sands, J. Appl. Phys. **105**, 024909 (2009).
[36] B. Saha, Y. R. Koh, J. P. Feser, S. Sadasivam, T. S. Fisher, A. Shakouri, and T. D. Sands, J. Appl. Phys. **121**, 015109 (2017).
[37] A. B. Mei, M. Tuteja, D. G. Sangiovanni, R. T. Haasch, A. Rockett, L. Hultman, I. Petrov, and J. E. Greene, J. Mater. Chem. C **4**, 7924 (2016).
[38] A. B. Mei, R. B. Wilson, D. Li, D. G. Cahill, A. Rockett, J. Birch, L. Hultman, J. E. Greene, and I. Petrov, J. Appl. Phys. **115**, 214908 (2014).
[39] W. Lengauer and P. Ettmayer, Monatshefte Chem. / Chem. Mon. **117**, 713 (1986).
[40] T. Lee, K. Ohmori, C. S. Shin, D. G. Cahill, I. Petrov, and J. E. Greene, Phys. Rev. B **71**, 144106 (2005).
[41] B. R. Zhao, L. Chen, H. L. Luo, M. D. Jack, and D. P. Mullin, Phys. Rev. B **29**, 6198 (1984).
[42] R. C. Powell, N. E. Lee, Y. W. Kim, and J. E. Greene, J. Appl. Phys. **73**, 189 (1993).
[43] C.-S. Shin, S. Rudenja, D. Gall, N. Hellgren, T.-Y. Lee, I. Petrov, and J. E. Greene, J. Appl. Phys. **95**, 356 (2004).
[44] H.-S. Seo, T.-Y. Lee, J. G. Wen, I. Petrov, J. E. Greene, and D. Gall, J. Appl. Phys. **96**, 878 (2004).
[45] D. G. Cahill, Rev. Sci. Instrum. **75**, 5119 (2004).
[46] K. Kang, Y. K. Koh, C. Chiritescu, X. Zheng, and D. G. Cahill, Rev. Sci. Instrum. **79**, 114901 (2008).
[47] Y. Wang, J. Y. Park, Y. K. Koh, and D. G. Cahill, J. Appl. Phys. **108**, 043507 (2010).
[48] R. M. Costescu, M. A. Wall, and D. G. Cahill, Phys. Rev. B **67**, 054302 (2003).

[49] Y. K. Koh, S. L. Singer, W. Kim, J. M. O. Zide, H. Lu, D. G. Cahill, A. Majumdar, and A. C. Gossard, J. Appl. Phys. **105**, 054303 (2009).
[50] M. W. Chase, *NIST-JANAF Thermochemical Tables*, 4th ed. (American Institute of Physics, Woodbury, NY, 1998), Monograph 9.
[51] A. M. Hofmeister, Phys. Chem. Miner. **41**, 361 (2014).
[52] V. F. Litvinenko, A. S. Bolgar, V. I. Kas'yan, L. K. Shvedova, and I. I. Timofeeva, Powder Metal. Met. Ceram. **19**, 109 (1980).
[53] A. Glaser, S. Surnev, F. P. Netzer, N. Fateh, G. A. Fontalvo, and C. Mitterer, Surf Sci. **601**, 1153 (2007).
[54] S. C. Weaver, An investigation of the thermal conductivity, electrical resistivity, and thermoelectric power of thorium nitride-uranium nitride alloys, Ph.D. thesis, University of Tennessee, 1972.
[55] L. Glasser and J. Hoy, J. Phys. Chem. **70**, 281 (1966).
[56] D. D. Betts, A. B. Bhatia, and M. Wyman, Phys. Rev. **104**, 37 (1956).
[57] C. S. Smith and E. Palmer, Trans AIME Papers **221**, 225 (1935).
[58] X. Zheng, D. G. Cahill, P. Krasnochtchekov, R. S. Averback, and J. C. Zhao, Acta Mater. **55**, 5177 (2007).
[59] T. M. Tritt, *Thermal Conductivity: Theory, Properties, and Applications* (Springer, New York, 2006).
[60] A. Wilson, *Mathematical Proceedings of the Cambridge Philosophical Society* (Cambridge University Press, Cambridge, 1937), p. 371.
[61] R. K. Williams, R. S. Graves, T. L. Hebble, D. L. McElroy, and J. P. Moore, Phys. Rev. B **26**, 2932 (1982).
[62] G. Grimvall, *The Electron-Phonon Interaction in Metals* (North-Holland, Amsterdam, 1981), Vols. 8 and 9.
[63] F. L. Madarasz and P. G. Klemens, Int. J. Thermophys. **8**, 257 (1987).
[64] V. Ambegaokar, Phys. Rev. **114**, 488 (1959).